Optical Engineering

OpticalEngineering.SPIEDigitalLibrary.org

Photogating for small high-responsivity graphene middle-wavelength infrared photodetectors

Shoichiro Fukushima
Masaaki Shimatani
Satoshi Okuda
Shinpei Ogawa
Yasushi Kanai
Takao Ono
Koichi Inoue
Kazuhiko Matsumoto

SPIE.

Shoichiro Fukushima, Masaaki Shimatani, Satoshi Okuda, Shinpei Ogawa, Yasushi Kanai, Takao Ono, Koichi Inoue, Kazuhiko Matsumoto, "Photogating for small high-responsivity graphene middle-wavelength infrared photodetectors," *Opt. Eng.* **59**(3), 037101 (2020), doi: 10.1117/1.OE.59.3.037101

Photogating for small high-responsivity graphene middle-wavelength infrared photodetectors

Shoichiro Fukushima,[a] Masaaki Shimatani,[a] Satoshi Okuda,[a] Shinpei Ogawa,[a,*] Yasushi Kanai,[b] Takao Ono,[b] Koichi Inoue,[b] and Kazuhiko Matsumoto[b]

[a]Mitsubishi Electric Corporation, Advanced Technology R&D Center, Amagasaki, Hyogo, Japan

[b]Osaka University, Institute of the Scientific and Industrial Research, Ibaraki, Osaka, Japan

Abstract. We demonstrated a middle-wavelength infrared (MWIR) graphene photodetector using the photogating effect. This effect was induced by photosensitizers situated around a graphene channel that coupled incident light and generated a large electrical charge. The graphene-based MWIR photodetector consisted of a top graphene channel, source–drain electrodes, an insulator layer, and a photosensitizer, and its photoresponse characteristics were determined by current measurements. Irradiation of the graphene channel of the vacuum cooled device by an MWIR laser generated a clear photoresponse, as evidenced by modulation of the output current during irradiation. The MWIR photoresponse with the photogating effect was 100 times greater than that obtained from conventional graphene photodetectors without the photogating effect. The device maintained its MWIR photoresponse at temperatures up to 150 K. The effect of the graphene channel size on the responsivity was evaluated to assess the feasibility of reducing the photodetector area, and decreasing the channel area from 100 to 25 μm^2 improved the responsivity from 61.7 to 321.0 AW^{-1}. The results obtained in our study will contribute to the development of high-performance graphene-based IR imaging sensors. [DOI: 10.1117/1.OE.59.3.037101]

Keywords: graphene; graphene photodetector; field effect transistor; infrared sensor; middle-wavelength infrared.

Paper 191602 received Nov. 14, 2019; accepted for publication Feb. 28, 2020; published online Mar. 18, 2020.

1 Introduction

Infrared (IR) imaging has been employed in a wide range of applications.[1] The 3- to 5-μm spectral band corresponding to the middle-wavelength IR (MWIR) region is especially important with regard to IR imaging, because this band is associated with commonly encountered temperatures. The 8- to 14-μm band corresponding to the long wavelength IR (LWIR) region is also important. The tracking of hot bodies (>300°C), aerial and satellite reconnaissance, and gas detection[2] using the MWIR region are currently performed with either thermal or quantum photodetectors. Thermal photodetectors respond to IR radiation by converting temperature changes into electronic signals and have the advantages of being inexpensive and operable at room temperature. However, the responsivity and response time of these devices are inferior to those of quantum detectors, which respond to IR light via a photoelectric conversion process. However, although quantum detectors provide superior responsivity, they contain toxic semiconductor materials such as mercury–cadmium–telluride. Therefore, there is a demand for low-cost, nontoxic, high-responsivity photomaterials so as to obtain the advantages of both types of IR photodetectors. Such materials would expand the range of applications of these devices.

Graphene has remarkable optoelectronic properties and thus could represent a means of improving photodetectors. As a result of its Dirac-cone band structure,[3,4] graphene exhibits

*Address all correspondence to Shinpei Ogawa, E-mail: Ogawa.Shimpei@eb.MitsubishiElectric.co.jp

broadband light absorption,[5–7] a rapid response,[8–12] gate-tunable plasmons,[13,14] and a strong nonlinear optical response.[15–17] In addition, graphene can be obtained at low cost through a nontoxic synthetic route, unlike quantum photomaterials.[18–20] Therefore, graphene photodetectors are expected to expand the range of IR applications due to these advantages. However, since graphene has a low light-absorption value of ∼2.3%,[21] a method is required to enhance the responsivity, such as the use of plasmonic antennas,[22] optical waveguides,[23] or photocarrier injection.[24] We have previously investigated various techniques for this purpose, including the use of p–n junctions,[25] plasmonic metamaterial absorbers,[26–28] and the photogating effect.[29–34] Here, we report a detailed mechanism for the photogating effect that significantly improves the responsivity of graphene photodetectors operating in the MWIR spectral band.

2 Device Fabrication and Assessment

Figure 1(a) shows a schematic illustration of the graphene photodetector used in this work, which is based on the design of a graphene field effect transistor (FET).[3,35] To produce this device, a p-type indium antimonide (InSb) substrate with a 260-nm-thick tetraethyl orthosilicate (TEOS) layer was initially prepared. Subsequently, source–drain electrodes made of 10-nm-thick Cr and 30-nm-thick Au layers were sputter deposited on the TEOS layer. The graphene was fabricated by chemical vapor deposition and then transferred onto the substrate on which the source–drain electrodes had been produced using a conventional graphene-transfer method.[36,37] Following this, a 5-μm-wide and 15-μm-long graphene channel was formed using a combination of photolithography and O_2 etching. Figure 1(b) presents the Raman spectrum obtained from this channel using a 512-nm excitation laser. The spectrum exhibits typical characteristics of graphene, including a G peak at 1580 cm^{-1} and a $2D$ peak at 2700 cm^{-1}, corresponding to the bond stretching and second-order breathing modes of sp^2 carbon atoms, respectively.[38–40] Therefore, this spectrum confirms that a monolayer graphene channel was successfully fabricated.

The responsivity of each graphene photodetector made during this study was investigated by electrical current measurements. In these trials, the device was positioned in a cooled vacuum probe system after which a source–drain voltage (V_{sd}) of 1.0 V and a back-gate voltage (V_{bg}) between −40 and 40 V were applied using a device analyzer. V_{bg} was applied to the back side of the substrate. Figure 2 plots the source–drain current (I_{sd}) as a function of V_{bg} for this device obtained at 77 K. Prior to these measurements, the Dirac point for each photodetector was tuned around a V_{bg} of ∼10 V by vacuum calcination at 423 K. The graphene channel was exposed to light emitted from a 1.6-μm diode fiber laser or to 4.6-, 8.0-, or 9.6-μm radiation from a quantum cascade laser. The photoresponse was calculated based on the extent of I_{sd} modulation between illuminated and dark conditions (photocurrent, $I_{photo} = I_{light} - I_{dark}$). The time-dependent current characteristics were measured with a dwell time of 80 ms and a 0.1-fA measurement resolution.

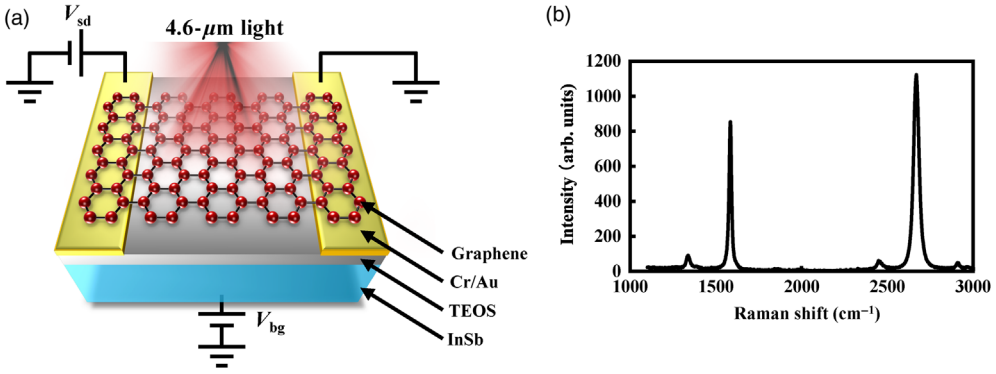

Fig. 1 (a) Schematic illustration of graphene-based photodetector design and (b) Raman spectrum of graphene channel.

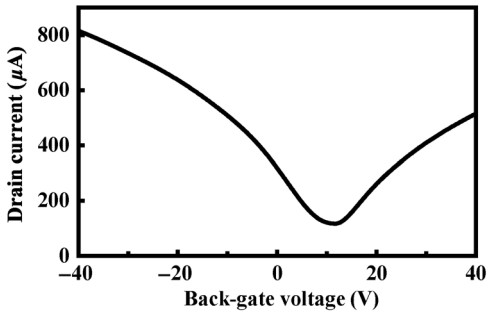

Fig. 2 Gating response of device.

3 Results and Discussion

3.1 *Photogating Modulation in MWIR Photoresponse*

The MWIR photoresponse of the graphene photodetector was initially investigated. Figure 3(a) shows the I_{photo} response of the device using a V_{sd} of 1.0 V and a V_{bg} of 0 V at 50 K. The device was exposed to the 4.6-μm laser in conjunction with a 2.0-s irradiation cycle (0.8 s on, 1.2 s off) and exhibited a definite photoresponse by generating an I_{photo} of 2.07 ± 0.02 μA during irradiation. Figure 3(b) shows the back-gate current (I_{bg}) during laser light irradiation. The photoresponse was associated with variations in I_{bg}, which in turn were modulated by the electrical charge in the InSb photosensitizer.

The effect of I_{sd} on V_{bg} was also investigated to further analyze the photogating effect. Figure 4(a) shows the experimentally determined gating responses under dark and illuminated conditions. The lowest I_{sd} was obtained at a V_{bg} of $\sim$10 V, which corresponds to the Dirac point for graphene. Figures 4(b)–4(d) present magnified views of the gating responses around V_{bg} values of 0 and 23.5 V, and Fig. 4(b) demonstrates an 87.0-mV change in the response at a V_{bg} of 0 V. In contrast, Figs. 4(c) and 4(d) show only a slight V_{bg} variation of 0.5 mV.

The photogating effect is primarily attributed to the behavior of photocarriers in the InSb photosensitizer. When a negative V_{bg} is applied to such a device, electron–hole pairs become separated in the p-doped InSb substrate, and the photoelectrons accumulate at the TEOS/InSb boundary. This surplus of electrons in the boundary region modulates the built-in electric field, which leads to the photogating effect. The results clearly indicate that the photogating effect enhances the photoresponse of the graphene by a factor of more than 100 compared with the inherent photoresponses of graphene obtained from photovoltaic,[10,25,41] bolometric,[35] and photothermoelectric effects.[42–44]

The photogating effect is achieved by modulating V_{bg} via photocarriers generated in the InSb substrate. The sequence of events by which the photoresponse of the device appears in conjunction with the photogating effect can be summarized as follows. First, during light irradiation at wavelengths shorter than the cutoff wavelength of the InSb substrate, electron–hole pairs (photocarriers) are generated in the InSb. These photoelectrons/holes are subsequently separated via

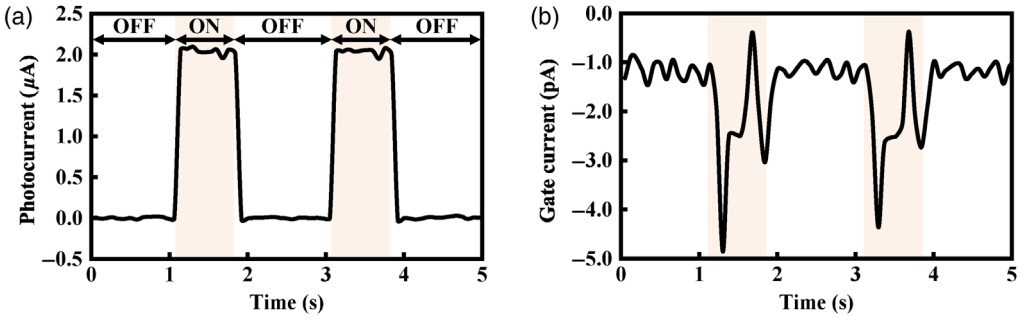

Fig. 3 Time-dependent (a) I_{photo} and (b) I_{bg} response of device under 4.6-μm pulsed laser irradiation.

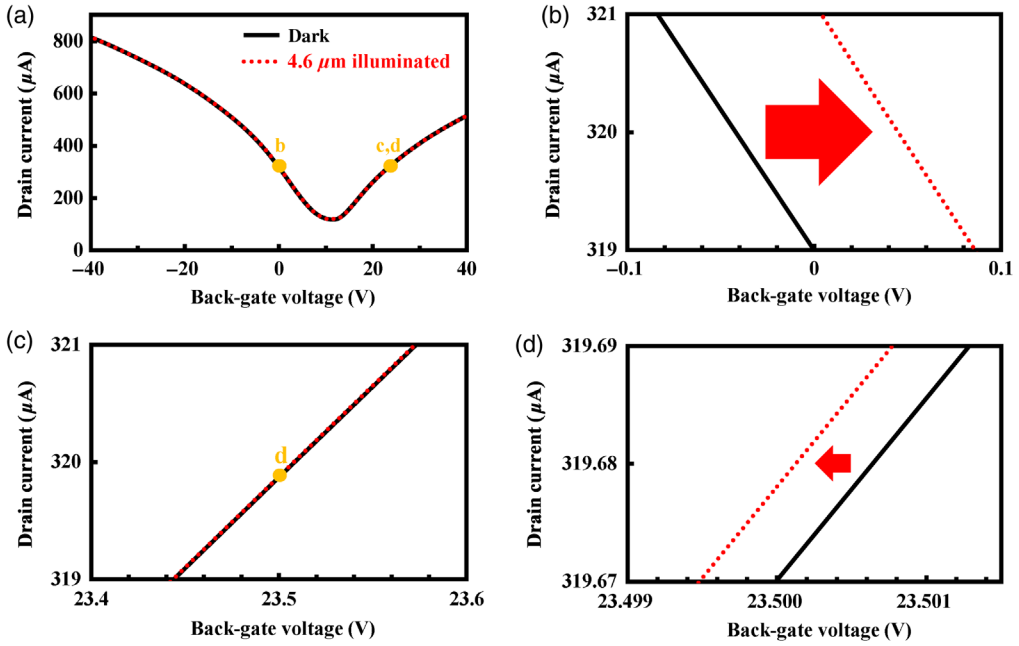

Fig. 4 (a) Gating responses under dark (black solid line) and 4.6-μm illuminated (red dotted line) conditions. (b)–(d) Magnified plots of drain current in vicinity of V_{bg} = (b) 0 and (c), (d) 23.5 V.

the application of V_{bg}. Second, the photoelectrons accumulate in the depletion layer at the TEOS/InSb boundary as a consequence of V_{bg},[29] and V_{bg} is modulated by the internal electric field generated by the accumulated photoelectrons. Third, the field effect in the graphene is changed by the modulation of V_{bg}. Specifically, variations in V_{bg} change the surface charge density of the graphene, and the corresponding change in the electrical signal from the graphene channel is detected as the photoresponse.

3.2 *Wavelength Dependence*

The wavelength dependence of the device performance was also investigated, and Fig. 5 shows the photoresponse of the device during pulsed laser light irradiation at 0.6, 1.6, 8.0, and 9.6 μm.

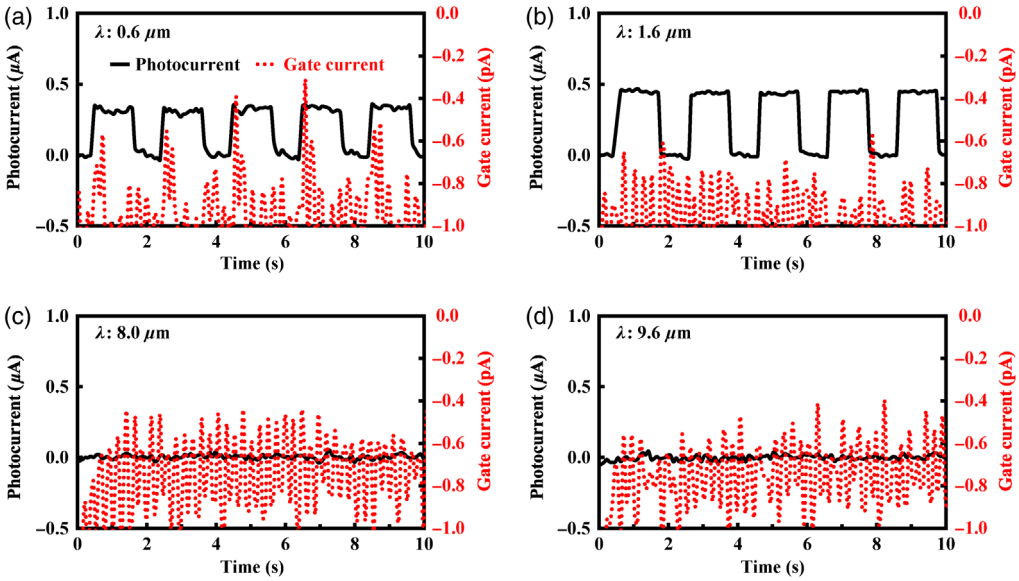

Fig. 5 Photoresponse of device at (a) 0.6, (b) 1.6, (c) 8.0, and (d) 9.6 μm.

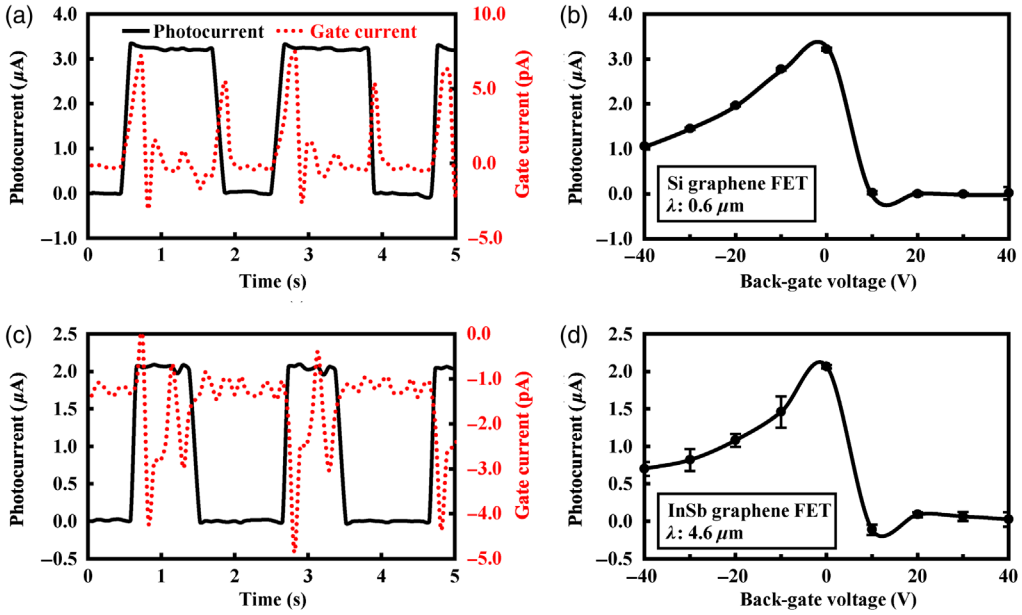

Fig. 6 (a), (b) Visible photoresponse of Si graphene FET at 293 K and (c), (d) MWIR photoresponse of InSb graphene FET at 50 K, showing (a), (c) time-dependent I_{photo} (black, solid) and gate current (red, dotted) and (b), (d) I_{photo} values as functions of back-gate voltage. Excitation wavelengths: (a), (b) 0.6 μm and (c), (d) 4.6 μm. Pulse periods: (a) 1.2 s on, 0.8 s off and (c) 0.8 s on, 1.2 s off.

The device evidently exhibited a photoresponse with I_{bg} modulation under irradiation at 0.6 and 1.6 μm. However, the photoresponse of the device was found to decrease significantly at longer wavelengths such that, as shown in Figs. 5(c) and 5(d); no photoresponse was obtained during irradiation in the LWIR region at 8.0 and 9.6 μm.

The photoresponse data obtained from a Si-based graphene FET were compared with those from an InSb-based graphene FET with both p-doped photosensitizers. A clear photoresponse was confirmed under irradiation at wavelengths shorter than the cutoff wavelength of the photosensitizer for both devices. Figure 6 presents the visible light photoresponse of the Si graphene FET and the MWIR photoresponse of the InSb graphene FET. The Si-based device produced a photoresponse under visible light irradiation [Figs. 6(a) and 6(b)], and the photoresponse characteristics together with the distinct back-gate voltage profile indicate the exact same behavior as that for the InSb-based graphene FET under MWIR irradiation [Figs. 6(c) and 6(d)].

At wavelengths longer than the bandgap wavelength, the photoresponses of both devices were decreased significantly. The MWIR and LWIR photoresponses of the Si-based graphene FET were especially weak, in the vicinity of only several mA/W. We also ascertained that the InSb-based graphene FET did not exhibit a photoresponse under LWIR light irradiation. In addition, generation of photocarriers in the photosensitizers under longer wavelength light was not evident, based on modulation of the gate current. Therefore, it can be concluded that the MWIR photoresponse of the InSb-based graphene FET was enhanced by the photogating effect.

3.3 *Temperature Dependence*

The effect of temperature on the MWIR photoresponse was assessed, and Fig. 7 shows the photoresponses obtained from the device at 150 and 200 K. At 150 K, the photogating effect was weakened by the generation of hot carriers, and so the inherent photoresponse of the graphene itself played the dominant role. At 200 K, I_{photo} was evidently not synchronized with the laser pulses. In addition, I_{bg} exhibited greater fluctuations in response to thermally generated carriers during pulsed irradiation compared with fluctuations at lower temperatures. Consequently, the photogating effect was weakened and an MWIR photoresponse could not be confirmed. At high temperatures, hot carriers would be expected to be generated in the InSb substrate as

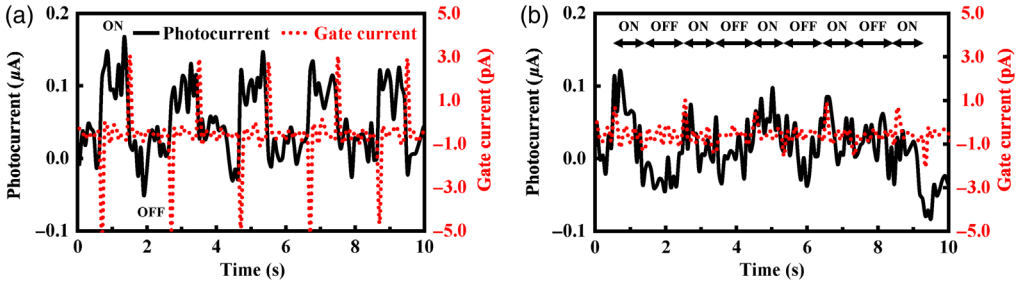

Fig. 7 Time dependence of I_{photo} (black solid lines) and I_{bg} (red dotted lines) for device at (a) 150 and (b) 200 K.

a consequence of thermal excitation, leading to changes in V_{bg} due to the varying concentrations of photocarriers.

3.4 *Device-Size Dependence*

The effect of the graphene channel dimensions on the MWIR photoresponse was also evaluated. Figure 8 plots the photoresponses of two devices having different channel aspect ratios but the same total channel area of 100 μm^2. The photoresponse is seen to increase from 1.15 ± 0.02 to 4.90 ± 0.39 μA upon increasing the ratio of the width (W) of the channel to its length (L) of gap between electrodes. The devices operate under the same principles as metal–oxide–semiconductor FETs, so changing the W/L ratio causes a resistance change in the graphene channel.

The effects of the graphene channel shape on the MWIR photoresponse were evaluated in more detail, and Fig. 9 plots I_{photo} for W/L ratios from 0.25 to 8.00. It is noteworthy that these I_{photo} values have been normalized with respect to the graphene field effect mobility (μ_{FE}), because μ_{FE} varied slightly even though the Dirac point for all devices was tuned to be about the same at 0 to 10 V. Assigning a value of 1 to I_{photo} for an aspect ratio of 8, I_{photo} values of 0.04, 0.08, 0.17, 0.26, 0.49, and 0.66 were obtained for aspect ratios of 0.25, 0.5, 1, 2, 4, and 6, respectively. It is evident that the resulting plot describes an almost linear correlation between I_{photo} and the aspect ratio of the channel. This line can be fit using the exponential expression shown in the figure. The results indicate that the MWIR photoresponse was affected by the shape of the graphene channel but not by the irradiated area or the total incident light power.

Figure 10(a) shows the MWIR responses of devices with channels having a fixed width of 5 μm and lengths of 5, 10, 15, or 20 μm. The responsivity was calculated from the photocurrent, the incident light intensity of 46.2 $\mu W/mm^2$, and the irradiated surface area, which is determined by the graphene channel size and the photocarrier diffusion distance in the InSb photosensitizers. The responsivity increases significantly with decreasing channel area, with values of 61.7, 68.1, 159.1, and 321.0 A/W corresponding to areas of 100, 75, 50, and 25 μm^2, respectively.

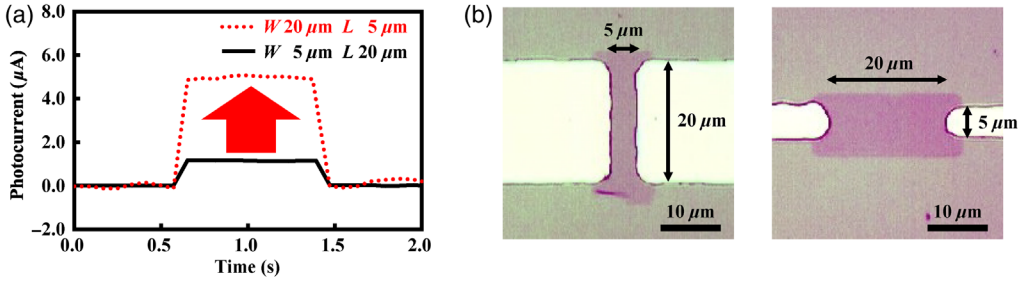

Fig. 8 (a) Time dependence of I_{photo} for devices with different graphene channel widths (W) and lengths (L). Black solid line: $W = 5$ μm, $L = 20$ μm right image in (b). Red dotted line: $W = 20$ μm, $L = 5$ μm left image in (b). Optical microscopy images of graphene channels.

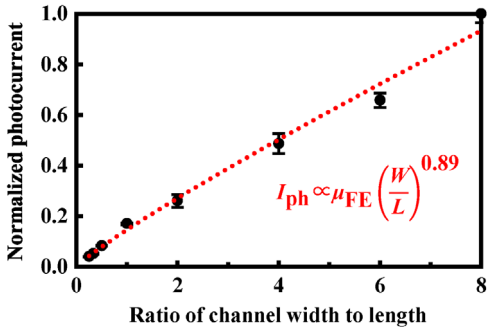

Fig. 9 Normalized I_{photo} values of devices with different aspect ratios.

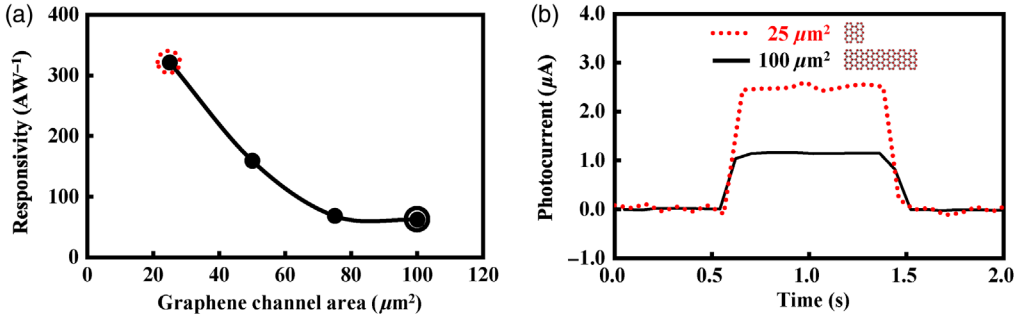

Fig. 10 (a) MWIR responsivity of devices with different graphene channel areas and (b) I_{photo} values over time for devices with 100-μm^2 (black solid line) and 25-μm^2 (red dotted line) graphene channel areas from which the data in (a) were obtained.

In general, the responsivity of a conventional photodetector is proportional to the irradiated area, because incident light energy is directly converted to a signal current/bias. In contrast, the photoresponse of a graphene photodetector using the photogating effect is not based on the direct collection of photoelectrons/holes from the photosensitizers but on modulation of the field effect around the graphene channel. A sufficiently strong field-effect modulation can be obtained via the localized accumulation of photoelectrons/holes in a depletion layer. Therefore, expansion of the irradiated area is not required in order to enhance the responsivity of such devices. A decrease in the graphene channel area leads to a change in the aspect ratio, which causes an increase in the photocurrent. The results of this work demonstrate that increasing the aspect ratio of the graphene channel decreases the device area and also improves the responsivity.

4 Conclusion

In conclusion, high-responsivity graphene photodetectors that operate in the MWIR spectral band based on the photogating effect were demonstrated. These devices consisted of a top graphene channel, source–drain electrodes, an insulator layer, and photosensitizers. An analysis of the effects of the irradiation wavelength and the photosensitizer on the photoresponse demonstrated that the photogating effect was induced by photosensitizers located around the graphene channel, as these materials couple incident light to generate a significant electrical charge. The MWIR photoresponse obtained in conjunction with the photogating effect was 2 orders of magnitude greater than that observed for conventional graphene photodetectors without this effect. The MWIR photoresponse was also found to be maintained at temperatures up to 150 K. The dimensions of the graphene channel were found to affect the photoresponse, showing that additional increases in photoresponse are possible via decreases in the device area. The results of this work are expected to assist in the future design and development of high-performance graphene-based IR imaging sensors.

Acknowledgments

This work was partially supported by the Innovative Science and Technology Initiative for Security, ATLA, Japan.

References

1. M. Vollmer and K.-P. Mollmann, *Infrared Thermal Imaging: Fundamentals, Research and Applications*, Wiley-VCH, Weinheim, Germany (2010).
2. H. Budzier and G. Gerlach, *Thermal Infrared Sensors: Theory, Optimisation and Practice*, John Wiley & Sons, Ltd., West Sussex (2011).
3. K. S. Novoselov et al., "Electric field effect in atomically thin carbon films," *Science* **306**(5696), 666–669 (2004).
4. K. S. Novoselov et al., "Two-dimensional gas of massless Dirac fermions in graphene," *Nature* **438**(7065), 197–200 (2005).
5. G. Pirruccio et al., "Coherent and broadband enhanced optical absorption in graphene," *ACS Nano* **7**(6), 4810–4817 (2013).
6. S. Ogawa et al., "Broadband photoresponse of graphene photodetector from visible to long-wavelength infrared wavelengths," *Opt. Eng.* **58**(5), 057106 (2019).
7. T. Wu, Y. Luo, and L. Wei, "Mid-infrared sensing of molecular vibrational modes with tunable graphene plasmons," *Opt. Lett.* **42**(11), 2066–2069 (2017).
8. F. Xia et al., "Ultrafast graphene photodetector," *Nat. Nanotechnol.* **4**(12), 839–843 (2009).
9. Y. M. Lin et al., "100-GHz transistors from wafer-scale epitaxial graphene," *Science* **327**(5966), 662–662 (2010).
10. T. Mueller, F. Xia, and P. Avouris, "Graphene photodetectors for high-speed optical communications," *Nat. Photonics* **4**(5), 297–301 (2010).
11. X. Gan et al., "Chip-integrated ultrafast graphene photodetector with high responsivity," *Nat. Photonics* **7**(11), 883–887 (2013).
12. X. Guo et al., "High-performance graphene photodetector using interfacial gating," *Optica* **3**(10), 1066–1070 (2016).
13. J. Chen et al., "Optical nano-imaging of gate-tunable graphene plasmons," *Nature* **487**(7405), 77–81 (2012).
14. B. Yao et al., "Broadband gate-tunable terahertz plasmons in graphene heterostructures," *Nat. Photonics* **12**(1), 22–28 (2018).
15. E. Hendry et al., "Coherent nonlinear optical response of graphene," *Phys. Rev. Lett.* **105**(9), 097401 (2010).
16. S. Shareef, Y. S. Ang, and C. Zhang, "Room-temperature strong terahertz photon mixing in graphene," *J. Opt. Soc. Am. B* **29**(3), 274–279 (2012).
17. K. J. A. Ooi et al., "Electronic scattering of graphene plasmons in the terahertz nonlinear regime," *IEEE J. Sel. Top. Quantum Electron.* **23**(4), 1–6 (2017).
18. L. Gao, J. R. Guest, and N. P. Guisinger, "Epitaxial graphene on Cu(111)," *Nano Lett.* **10**(9), 3512–3516 (2010).
19. D. Ding et al., "Behavior and role of superficial oxygen in Cu for the growth of large single-crystalline graphene," *Appl. Surf. Sci.* **408**, 142–149 (2017).
20. X. Li et al., "Transfer of large-area graphene films for high-performance transparent conductive electrodes," *Nano Lett.* **9**(12), 4359–4363 (2009).
21. R. R. Nair et al., "Fine structure constant defines visual transparency of graphene," *Science* **320**(5881), 1308 (2008).
22. Y. Yao et al., "High-responsivity mid-infrared graphene detectors with antenna-enhanced photocarrier generation and collection," *Nano Lett.* **14**(7), 3749–3754 (2014).
23. J. Wang et al., "High-responsivity graphene-on-silicon slot waveguide photodetectors," *Nanoscale* **8**(27), 13206–13211 (2016).
24. G. Konstantatos et al., "Hybrid graphene–quantum dot phototransistors with ultrahigh gain," *Nat. Nanotechnol.* **7**, 363–368 (2012).
25. M. Shimatani et al., "Photocurrent enhancement of graphene phototransistors using p-n junction formed by conventional photolithography process," *Jpn. J. Appl. Phys.* **55**(11), 110307 (2016).

26. S. Ogawa, D. Fujisawa, and M. Ueno, "Effect of graphene on plasmonic metasurfaces at infrared wavelengths," *AIP Adv.* **3**(11), 112127 (2013).
27. S. Ogawa et al., "Graphene on metal–insulator–metal-based plasmonic metamaterials at infrared wavelengths," *Opt. Express* **26**(5), 5665–5674 (2018).
28. M. Shimatani et al., "Multispectral graphene infrared photodetectors using plasmonic metasurfaces," *Proc. SPIE* **11002**, 1100224 (2019).
29. M. Shimatani et al., "Giant Dirac point shift of graphene phototransistors by doped silicon substrate current," *AIP Adv.* **6**(3), 035113 (2016).
30. S. Fukushima et al., "High responsivity middle-wavelength infrared graphene photodetectors using photo-gating," *Appl. Phys. Lett.* **113**(6), 061102 (2018).
31. M. Shimatani et al., "Enhanced photogating via pyroelectric effect induced by insulator layer for high-responsivity long-wavelength infrared graphene-based photodetectors operating at room temperature," *Appl. Phys. Express* **12**(2), 025001 (2019).
32. S. Fukushima et al., "High-responsivity graphene infrared photodetectors using photogating effect," *Proc. SPIE* **11002**, 1100223 (2019).
33. S. Fukushima et al., "Low dark current and high-responsivity graphene mid-infrared photodetectors using amplification of injected photo-carriers by photo-gating," *Opt. Lett.* **44**(10), 2598–2601 (2019).
34. M. Shimatani et al., "High-responsivity turbostratic stacked graphene photodetectors using enhanced photogating," *Appl. Phys. Express* **12**(12), 122010 (2019).
35. J. B. Oostinga et al., "Gate-induced insulating state in bilayer graphene devices," *Nat. Mater.* **7**(2), 151–157 (2008).
36. J. W. Suk et al., "Transfer of CVD-grown monolayer graphene onto arbitrary substrates," *ACS Nano* **5**(9), 6916–6924 (2011)
37. K. Uemura, T. Ikuta, and K. Maehashi, "Turbostratic stacked CVD graphene for high-performance devices," *Jpn. J. Appl. Phys.* **57**(3), 030311 (2018).
38. A. C. Ferrari et al., "Raman spectrum of graphene and graphene layers," *Phys. Rev. Lett.* **97**(18), 187401 (2006).
39. J.-S. Hwang et al., "Imaging layer number and stacking order through formulating Raman fingerprints obtained from hexagonal single crystals of few layer graphene," *Nanotechnology* **24**(1), 015702 (2012).
40. A. Reina et al., "Transferring and identification of single- and few-layer graphene on arbitrary substrates," *J. Phys. Chem. C* **112**(46), 17741–17744 (2008).
41. T. J. Echtermeyer et al., "Strong plasmonic enhancement of photovoltage in graphene," *Nat. Commun.* **2**(1), 458 (2011).
42. J. C. Song et al., "Hot carrier transport and photocurrent response in graphene," *Nano Lett.* **11**(11), 4688–4692 (2011).
43. N. M. Gabor et al., "Hot carrier-assisted intrinsic photoresponse in graphene," *Science* **334**(6056), 648–652 (2011).
44. D. Sun et al., "Ultrafast hot-carrier-dominated photocurrent in graphene," *Nat. Nanotechnol.* **7**(2), 114–118 (2012).

Biographies of the authors are not available.